




Cite this: *RSC Adv.*, 2020, 10, 9335

# An integrated electrode based on nanoflakes of MoS<sub>2</sub> on carbon cloth for enhanced lithium storage†

Yan Guo, \* Shuang Li, Qiuyue Fang, Jialu Zuo, Ming Liu and Jun Zhang \*

Due to its high specific capacity (in theory), molybdenum disulfide (MoS<sub>2</sub>) has been recognized as a plausible substitute in lithium-ion batteries (LIBs). However, it suffers from an inferior electric conductivity and a substantial volume change during Li<sup>+</sup> insertion/extraction. By using a facile hydrothermal method, a flexible free-standing MoS<sub>2</sub> electrode has here been fabricated onto a carbon cloth substrate. The grafting of ultrathin MoS<sub>2</sub> nanoflakes onto the carbon cloth framework (forming CC@MoS<sub>2</sub>), was shown to facilitate an improved electron transport, as well as an enhanced Li<sup>+</sup> transport. As expected, the as-obtained CC@MoS<sub>2</sub> electrode was observed to exhibit an excellent lithium storage performance. It delivers a high discharge specific capacity of 2.42 mA h cm<sup>-2</sup> at 0.7 mA cm<sup>-2</sup> (even after 100 cycles), which is an impressive result.

Received 20th December 2019  
Accepted 22nd February 2020

DOI: 10.1039/c9ra10756h

rsc.li/rsc-advances

## 1. Introduction

In recent years, the rapid advances in the field of flexible and portable devices (such as flexible smartphones, rollup displays and wearable electronics) have triggered the requirements for flexible energy storage systems with excellent mechanical and electrical properties.<sup>1–5</sup> For instance, with the development of implantable/wearable healthcare devices, new self-sustainable energy storage devices have been developed.<sup>6</sup> Amongst the available commercial power sources, flexible lithium-ion batteries (LIBs) have attracted a special attention. This is due to their large energy density (with lightweight and easy portability), and long-life cycle.<sup>7</sup> So flexible lithium-ion batteries are able to be embedded into these soft portable electronic devices and power them. The key challenge is to design flexible electrode materials with excellent electrochemical performance. However, the fabrication of conventional LIB electrodes most often requires the introduction of conductive additives and binders. It cannot therefore meet the requirements to produce flexible devices. The development of integrated electrode materials, with excellent conductivity and flexibility, is therefore crucial for the utilization of flexible LIBs in portable devices.<sup>8,9</sup>

Molybdenum disulfide (MoS<sub>2</sub>), with a two-dimensional (2D) graphene-like structure and a high theoretical capacity of 670 mA h g<sup>-1</sup>, is a well-known anode material for LIBs. The large interlayer spacing (~0.62 nm) offers a permeable path to promote Li<sup>+</sup> transport during the charge/discharge process.<sup>10,11</sup>

Nevertheless, the electrochemical performance of bulk MoS<sub>2</sub>-based electrodes is not satisfying. The major bottleneck is the capacity degradation and poor rate performance in practical applications, which is caused by the intrinsic low electrical conductivity and large volume expansion upon cycling.<sup>12–14</sup> Hence, additional components, such as conductive additives, binders and current collectors, are usually required for the preparation of electrodes. However, this leads to lower gravimetric capacity, power density, and energy density.<sup>15</sup> To address these issues, one of the strategies is to construct MoS<sub>2</sub> in combination with flexible and conductive substrates.<sup>1,10,14,16–20</sup> However, the complex preparation process of these integrated electrodes is still a major obstacle. It is therefore necessary to further optimize the synthesis process of MoS<sub>2</sub>-based flexible electrodes by using a facile and low-cost technique that is suitable for flexible electronic devices with enhanced electrochemical performances.

A carbon cloth (CC), with its high electron conductivity, flexibility and superior mechanical property, is regarded to be one of the ideal substrates for the fabrication of flexible electrodes.<sup>2,9,21</sup> Thus, the integration of MoS<sub>2</sub> with conductive CC will guarantee the combination of fast electron transport and superior mechanical stability.<sup>22–24</sup>

The prerequisites for the design and preparation of an integrated electrode has been studied in the present investigation. Ultrathin MoS<sub>2</sub> nanoflakes were anchored on top of the carbon cloth substrate by using a hydrothermal approach (denoted as CC@MoS<sub>2</sub>). With the benefit of a well-defined conductive network and ultrathin nanoflakes subunits, the CC@MoS<sub>2</sub> electrode is expected to have an outstanding lithium storage performance.

College of Chemistry and Chemical Engineering, Inner Mongolia University, Hohhot 010021, P. R. China. E-mail: guoyan@imu.edu.cn; cejzhang@imu.edu.cn

† Electronic supplementary information (ESI) available. See DOI: 10.1039/c9ra10756h



## 2. Experiments

### 2.1 Synthesis of CC@MoS<sub>2</sub>

The carbon cloth material (purchased from Aldrich) was first activated in concentrated sulfuric acid and nitric acids (at a temperature of 100 °C, and for a duration of 8 h). The acid-treated carbon cloth was thereafter washed with de-ionized (DI) water and dried for further use. L-Cysteine (0.25 g) was, under stirring, added to 20 mL of an aqueous solution containing Na<sub>2</sub>MoO<sub>4</sub>·2H<sub>2</sub>O (0.2 g), and thereafter transferred to a 30 mL Teflon-lined stainless-steel autoclave. The acid-treated carbon cloth was added to the solution in the autoclave and maintained in an oven at 220 °C for 24 h. After cooling down to room temperature, the as-prepared carbon cloth (*i.e.*, the CC@MoS<sub>2</sub>-precursor) was thoroughly washed with DI and dried overnight (at 70 °C). Crystalline CC@MoS<sub>2</sub> was thereafter obtained by placing the precursor in an atmosphere of gaseous H<sub>2</sub>/Ar (5% H<sub>2</sub>) at 700 °C for 2 h (with a heating rate of 1 °C min<sup>-1</sup>). The preparation process of MoS<sub>2</sub> particles was like the preparation of crystalline CC@MoS<sub>2</sub>, except for the addition of carbon cloth.

### 2.2 Characterization

The morphologies of the samples were characterized by using field-emission scanning electron microscopy (FESEM; Hitachi

S-4800), and transmission electron microscopy (TEM; FEI Tecnai F20). Energy-dispersive X-ray spectroscopy (EDX), with an instrument attached to the TEM instrument, was used for the analysis of the chemical composition. Moreover, X-ray diffraction (XRD) patterns were collected with the use of a PANalytical Empyrean diffractometer (with a Cu Kα1 radiation;  $\lambda = 1.5405 \text{ \AA}$ ). X-ray photoelectron spectroscopy (XPS; VG Scientific ESCALAB) was carried out with the C 1s peak as a reference (284.6 eV). Raman spectra were carried out by using the RENISHAW inVia Microscope Raman system with a wavelength of 532 nm.

### 2.3 Electrochemical measurements

The 2430-type coin cells were assembled in an Ar-filled glovebox by using the CC@MoS<sub>2</sub> material (in size of  $1 \times 1 \text{ cm}^2$ ) as the working electrode (without any conductive additives or binder). A lithium foil was used as the counter (and reference) electrode. 1.0 M LiPF<sub>6</sub>, in an ethylene carbonate/diethyl carbonate (50 : 50, w/w) solution, was used as an electrolyte. Galvanostatic discharge-charge tests were carried out by using a Land battery measurement system (Land, China). Moreover, cyclic voltammetry (CV) measurements were carried out with the use of an electrochemical workstation (CHI 660E).

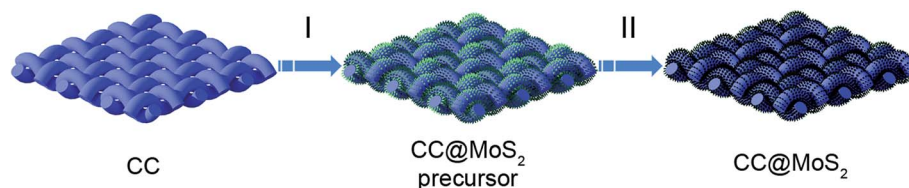


Fig. 1 Schematic illustration of the synthesis route of CC@MoS<sub>2</sub>. (I) Growth of MoS<sub>2</sub> nanoflakes on a CC backbone by using a hydrothermal strategy; (II) formation of CC@MoS<sub>2</sub> from thermal treatment.

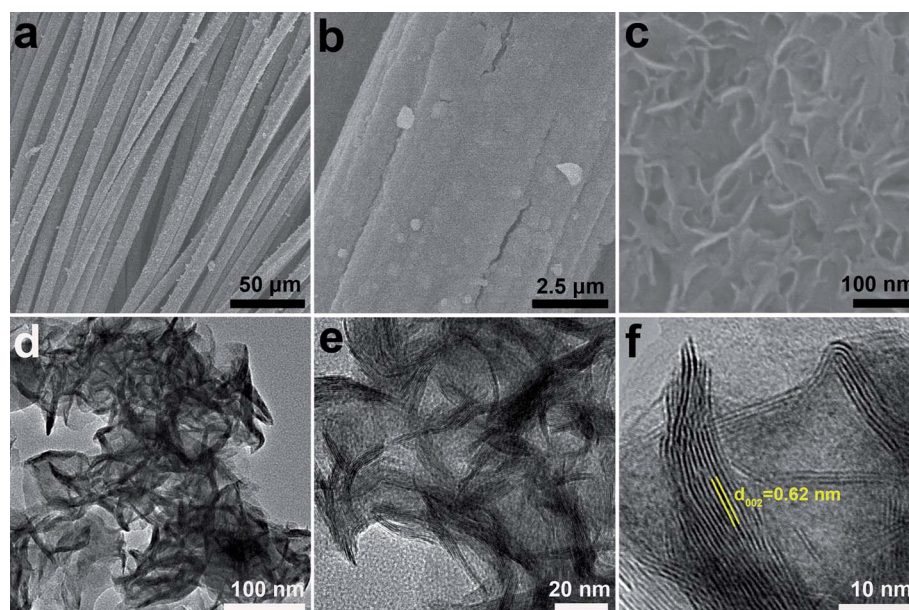


Fig. 2 (a–c) FESEM, (d and e) TEM and (f) HRTEM images of CC@MoS<sub>2</sub> after calcination.



### 3. Results and discussion

The strategy for the synthesis of the CC@MoS<sub>2</sub> material is schematically illustrated in Fig. 1. An ultrathin layer of MoS<sub>2</sub> nanoflakes was uniformly grown onto a smooth surface of carbon cloth by using an effective hydrothermal approach (step I). This step was followed by controlled calcination (step II), which lead to the formation of CC@MoS<sub>2</sub>. FESEM images of a bare carbon cloth surface reveal the smoothness of the surface (see Fig. S1, ESI†). It shows a typical interconnected network structure that is constructed by interwoven carbon fibers. As a result of the hydrothermal reaction, this CC surface became coated with a layer of dense and interconnected nanoflakes (Fig. S2a–c, ESI†). No bare CC fiber, or assemblies of MoS<sub>2</sub> nanoflakes, were observed. Furthermore, the structural features of the MoS<sub>2</sub> nanoflakes were characterized by using TEM and high resolution TEM (HRTEM) (Fig. S2d–f, ESI†). The analysis

showed that the MoS<sub>2</sub> layer consists of randomly oriented ultrathin nanoflakes with a total thickness of a few nanometers, which is consistent with the FESEM observation. Fig. S3† shows the XRD results for the CC@MoS<sub>2</sub> precursor. There are broadened diffraction peaks at 25.7° and 43.8°, which could be assigned to the CC substrate.<sup>25</sup> Moreover, there are no obvious sharp peaks of MoS<sub>2</sub>, which is an indication of low crystallinity. XPS measurements were used to study the valence state of Mo and S in CC@MoS<sub>2</sub> precursor (Fig. S4, ESI†). Two peaks at around 229.6 and 232.9 eV can be ascribed to Mo 3d<sub>5/2</sub> and Mo 3d<sub>3/2</sub>, respectively, revealing that molybdenum is in its Mo(IV) state.<sup>26,27</sup> Two peaks which are located at 162.6 and 163.7 eV can be ascribed to S 2p<sub>3/2</sub> and S 2p<sub>1/2</sub>, respectively.<sup>28</sup> These results indicate the presence of Mo<sup>4+</sup> and S<sup>2−</sup> species within the CC@MoS<sub>2</sub> precursor. The main feature of the structure and morphology was maintained even after the calcination process, as shown in Fig. 2. As observed in the FESEM images of

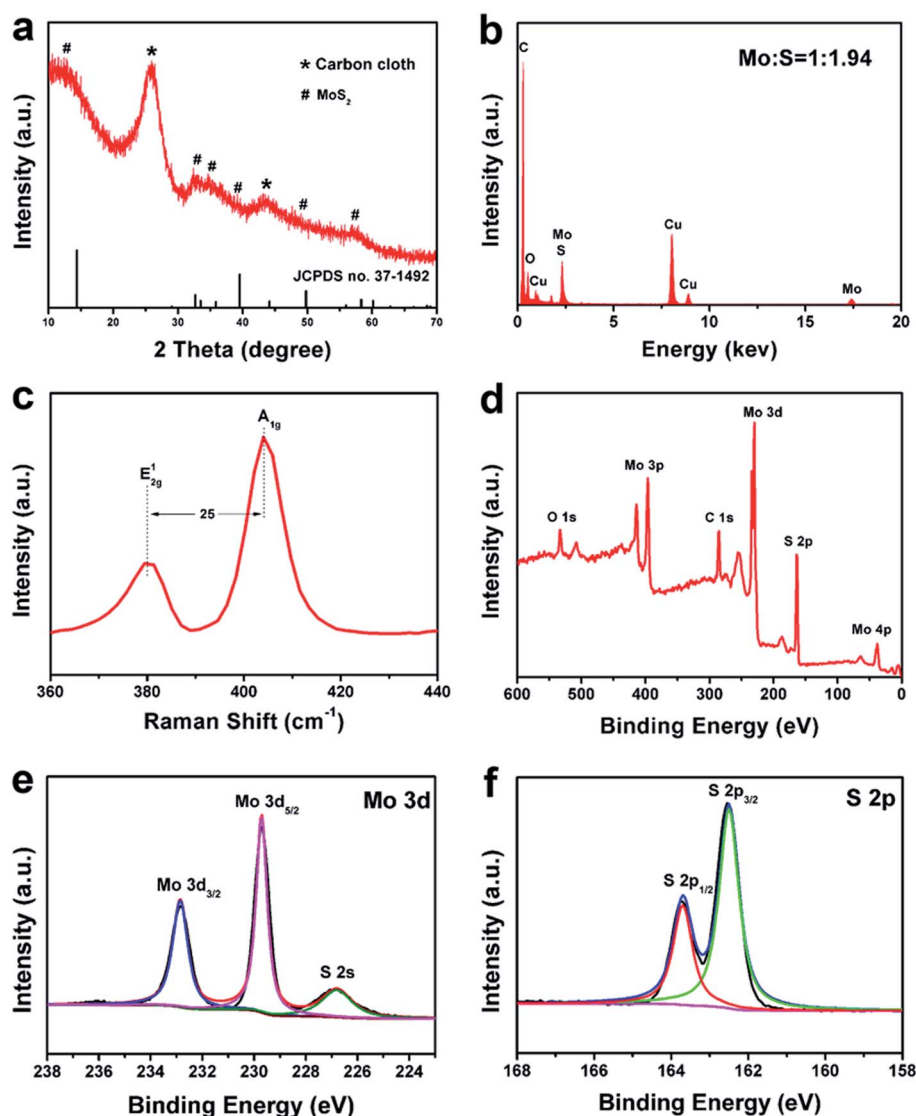


Fig. 3 (a) XRD pattern, (b) EDX spectrum, (c) Raman spectrum, and (d) XPS spectrum of the CC@MoS<sub>2</sub> material. High resolution XPS spectra showing the (e) Mo 3d, and the (f) S 2p regions for CC@MoS<sub>2</sub>.

calcinated CC@MoS<sub>2</sub> (Fig. 2a–c), as well as in the TEM images thereof (Fig. 2d and e), the overall surface of CC became homogeneous coated with MoS<sub>2</sub> nanoflakes. Moreover, the lattice fringes are clearly seen in the HRTEM image (Fig. 2f), where the interplanar distance of about 0.62 nm corresponds to the (002) facet of hexagonal MoS<sub>2</sub>. The selected-area electron diffraction (SAED) pattern (Fig. S5, ESI†) depicts well-defined rings, suggesting a polycrystalline structure of MoS<sub>2</sub>.<sup>29</sup> Compared with the CC@MoS<sub>2</sub> precursor, the CC@MoS<sub>2</sub> sample was observed to exhibit an improved crystalline structure after the annealing process (Fig. 3a). Three new diffraction peaks at about 14.41, 32.61, and 58.31 were observed, which can be ascribed to the (002), (100), and (110) planes of 2H-phase MoS<sub>2</sub> (JCPDS no. 37-1492), respectively.<sup>30,31</sup> Furthermore, EDX spectroscopy revealed that the atomic S/Mo ratio (in CC@MoS<sub>2</sub>) was about 1.94, which confirms the dominant MoS<sub>2</sub> phase (Fig. 3b). The successful preparation of MoS<sub>2</sub> in the CC@MoS<sub>2</sub> sample was further verified by the Raman spectroscopy characterization (Fig. 3c). The sample showed in-layer E<sub>2g</sub><sup>1</sup> and out-of-layer A<sub>1g</sub> Raman modes, which were located at 380 cm<sup>−1</sup> and 405 cm<sup>−1</sup>, respectively. This result confirms the existence of hexagonal MoS<sub>2</sub> in the CC@MoS<sub>2</sub> sample.<sup>23,29</sup> In addition, XPS analysis was performed in order to examine the chemical compositions and valence states. As depicted in Fig. 3d, the C, Mo, S, and O signals were observed in the overall XPS spectrum of the CC@MoS<sub>2</sub> sample. The corresponding high-resolution Mo 3d and S 2p spectra are shown in Fig. 3e and f. As can be seen in these latter spectra, there are two Mo 3d peaks and two S 2p peaks that correspond to Mo<sup>4+</sup> 3d<sub>5/2</sub> (~229.70 eV), Mo<sup>4+</sup> 3d<sub>3/2</sub> (~232.80 eV), S<sup>2−</sup> 2p<sub>3/2</sub> (~162.55 eV) and S<sup>2−</sup> 2p<sub>1/2</sub> (~163.75 eV),

respectively.<sup>1,29,32</sup> The peak at ~226.80 eV is assigned to the S<sup>2−</sup> 2s component of MoS<sub>2</sub>.<sup>1</sup> In addition, based on the XPS data, the atom percent of S 2p, Mo 3d, and C 1s in the CC@MoS<sub>2</sub> composites are about 28.69%, 15.6%, and 55.71%, respectively. All of the here presented measurements demonstrate a successful synthesis of the CC@MoS<sub>2</sub> composite material.

The electrochemical properties of the annealed CC@MoS<sub>2</sub> material, to be used as an anode material in LIBs, were also investigated. Fig. 4a shows the cycling performance of annealed CC@MoS<sub>2</sub>, and of bare MoS<sub>2</sub> nanoparticles, at a current density of 0.4 mA cm<sup>−2</sup>. As expected, the CC@MoS<sub>2</sub> material was observed to exhibit a high reversibility capacity of 2.75 mA h cm<sup>−2</sup> (without any obvious capacity decay after 50 cycles). From the second cycle and onwards, the CC@MoS<sub>2</sub> delivered a coulombic efficiency of more than 93%. For comparison, bare MoS<sub>2</sub> nanoparticles were prepared as the CC@MoS<sub>2</sub> material, except for the addition of carbon cloth. The capacity of the bare MoS<sub>2</sub> nanoparticles was found to be as low as 2.42 mA h cm<sup>−2</sup> at the second cycle, and the following decrease in capacity was much faster (compared to CC@MoS<sub>2</sub>). Fig. 4b demonstrates the galvanostatic discharge–charge voltage profiles for the CC@MoS<sub>2</sub> electrode. It is obtained at 0.7 mA cm<sup>−2</sup> and in the voltage range of 0.0–2.7 V vs. Li/Li<sup>+</sup>. During the first discharge process, there are two voltage plateaus at about 1.1 and 0.6 V. They correspond to Li<sup>+</sup> ions insertion into the interlayer of MoS<sub>2</sub> (forming the Li<sub>x</sub>MoS<sub>2</sub> intermediate), and the following Li<sub>x</sub>MoS<sub>2</sub> decomposition into metallic Mo and Li<sub>2</sub>S, respectively.<sup>10,13,33</sup> The overall chemical reaction of this discharge process can be described as follows: MoS<sub>2</sub> + 4Li<sup>+</sup> → Mo + 2Li<sub>2</sub>S.<sup>31</sup> In addition, Li<sup>+</sup> ions will be extracted from the Li<sub>2</sub>S

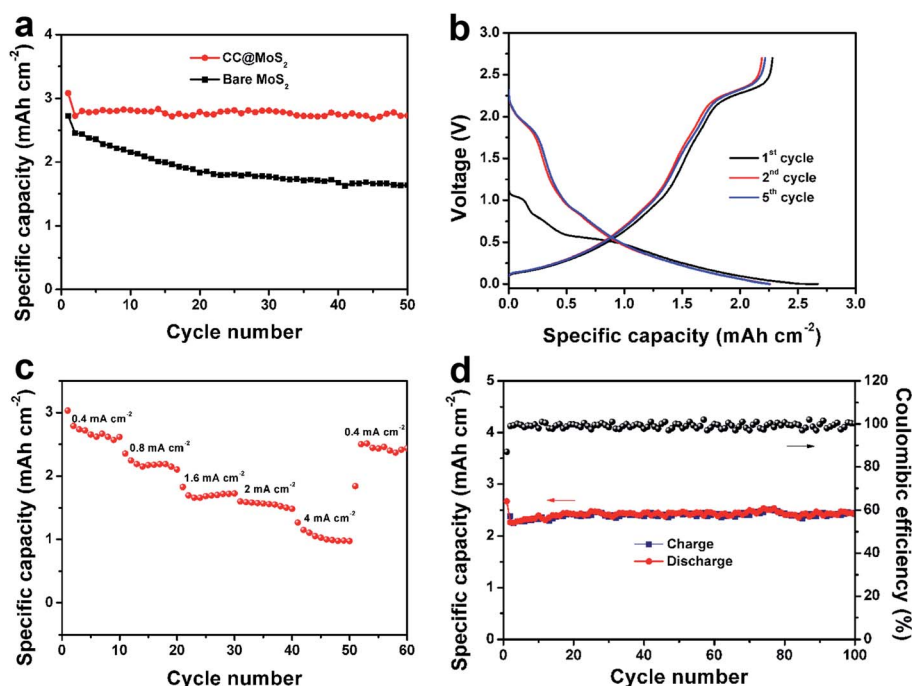


Fig. 4 Electrochemical performance of annealed CC@MoS<sub>2</sub>. (a) Cycling performance at 0.4 mA cm<sup>−2</sup> for annealed CC@MoS<sub>2</sub>, and for bare MoS<sub>2</sub> nanoparticles. (b) Discharge–charge voltage profiles for the 1<sup>st</sup>, 2<sup>nd</sup>, and 5<sup>th</sup> cycle at a current density of 0.7 mA cm<sup>−2</sup>. (c) Rate performance. (d) Cycling performance at a current density of 0.7 mA cm<sup>−2</sup>.



matrix during the charging process.<sup>10</sup> By using the CC@MoS<sub>2</sub> electrode, CV curves for the 1<sup>st</sup>, 2<sup>nd</sup> and 5<sup>th</sup> cycle, and at a scan rate of 0.05 mV s<sup>-1</sup>, are presented in Fig. S6 (see ESI†). Distinct peaks are in this figure observed, which are consistent with the plateaus observed in the discharge-charge voltage profiles (see Fig. 4b). Importantly, the CV curves do well overlap after the first cycle, suggesting a highly reversible and stable lithium storage process. Furthermore, the rate capability has also been investigated, as presented in Fig. 4c. The CC@MoS<sub>2</sub> electrode displays averaged reversible specific capacities of 2.75, 2.21, 1.74, 1.54, and 1.09 mA h cm<sup>-2</sup> at current densities of 0.4, 0.8, 1.6, 2, and 4 mA cm<sup>-2</sup>, respectively. Moreover, a large discharge specific capacity of 2.5 mA h cm<sup>-2</sup> was achieved when the current density returned to 0.4 mA cm<sup>-2</sup> (after 50 cycles). The cycling performance of the CC@MoS<sub>2</sub> electrode, at a current density of 0.7 mA cm<sup>-2</sup>, is shown in Fig. 4d. The electrode was found to deliver initial discharge and charge capacities of 2.67 and 2.38 mA h cm<sup>-2</sup>, respectively. The capacity loss is most probably caused by irreversible processes, such as decomposition of the electrolyte and formation of a solid-electrolyte interface layer.<sup>19,33</sup> After a slow decay in capacity, in the initial charge and discharge tests, the capacity was now found to remain stable. A high discharge specific capacity of 2.42 mA h cm<sup>-2</sup> was retained, even after 100 cycles. In addition, the coulombic efficiency was close to 100% during the entire cycling tests, which suggests an outstanding long-term cyclability. To analyze the structural stability of CC@MoS<sub>2</sub> electrodes during cycling process, the micrographs of CC@MoS<sub>2</sub> after cycling tests were recorded. As shown in Fig. S7,† the MoS<sub>2</sub> is still tightly coated on the surface of carbon cloth after 100 cycles at 0.7 mA cm<sup>-2</sup>.

In summary, the outstanding lithium storage properties are here mainly ascribed to the inherent merits of the CC@MoS<sub>2</sub> electrode. The strong anchoring of ultrathin MoS<sub>2</sub> nanoflakes onto a CC backbone will result in a large concentration of electroactive sites, and rapid transportation of electrolytes and ions.<sup>10</sup> Moreover, the CC backbone will not only provide a continuous electronic transport network for a rapid transfer of electrons. It will also efficiently accommodate the necessary strain (during cycling) that leads to an outstanding electrochemical stability.<sup>18</sup>

## 4. Conclusions

A facile hydrothermal method has here been presented, by which it is possible to construct an integrated electrode to be used in LIBs. The electrode material consists of an ultrathin layer of MoS<sub>2</sub> nanoflakes that are anchored on a CC backbone. The inherent merits of this CC@MoS<sub>2</sub> material convey a fast transport of electrons and ions for enhanced lithium storage. As a result, the hybrid anode exhibits the high reversible capacity of 2.42 mA h cm<sup>-2</sup> at 0.7 mA cm<sup>-2</sup> (even after 100 cycles). As compared to traditional electrode materials, the CC@MoS<sub>2</sub> electrode can be widely used in flexible and folded electronic products. This development will most probably initiate both novel applications, as well as constructions of a multitude of different types of flexible energy storage devices.

## Conflicts of interest

There are no conflicts to declare.

## Acknowledgements

This work was supported by the National Natural Science Foundation of China (Grant No. 21701090, 21975015), the Natural Science Foundation of Inner Mongolia Autonomous Region of China (Grant No. 2017BS0203), and the Program of Higher-level Talents of Inner Mongolia University (Grant No. 21300-5165154).

## References

- 1 Z.-H. Zhao, X.-D. Hu, H. Wang, M.-Y. Ye, Z.-Y. Sang, H.-M. Ji, X.-L. Li and Y. Dai, *Nano Energy*, 2018, **48**, 526–535.
- 2 Y. Han, Y. Lu, S. Shen, Y. Zhong, S. Liu, X. Xia, Y. Tong and X. Lu, *Adv. Funct. Mater.*, 2019, **29**, 1806329.
- 3 B. Yao, J. Zhang, T. Kou, Y. Song, T. Liu and Y. Li, *Adv. Sci.*, 2017, **4**, 1700107.
- 4 L. Zhu, D. Zheng, Z. Wang, X. Zheng, P. Fang, J. Zhu, M. Yu, Y. Tong and X. Lu, *Adv. Mater.*, 2018, **30**, 1805268.
- 5 X. Yan, Z. Liu, Q. Zhang, J. Lopez, H. Wang, H. C. Wu, S. Niu, H. Yan, S. Wang, T. Lei, J. Li, D. Qi, P. Huang, J. Huang, Y. Zhang, Y. Wang, G. Li, J. B. Tok, X. Chen and Z. Bao, *J. Am. Chem. Soc.*, 2018, **140**, 5280–5289.
- 6 D. P. Dubal, N. R. Chodankar, D. H. Kim and P. Gomez-Romero, *Chem. Soc. Rev.*, 2018, **47**, 2065–2129.
- 7 Y. Hu and X. Sun, *J. Mater. Chem. A*, 2014, **2**, 10712–10738.
- 8 L. Yu, J. F. Yang and X. W. Lou, *Angew. Chem., Int. Ed.*, 2016, **55**, 13422–13426.
- 9 J. He, N. Wang, Z. Cui, H. Du, L. Fu, C. Huang, Z. Yang, X. Shen, Y. Yi, Z. Tu and Y. Li, *Nat. Commun.*, 2017, **8**, 1172.
- 10 X. Hu, Y. Li, G. Zeng, J. Jia, H. Zhan and Z. Wen, *ACS Nano*, 2018, **12**, 1592–1602.
- 11 Z.-T. Shi, W. Kang, J. Xu, Y.-W. Sun, M. Jiang, T.-W. Ng, H.-T. Xue, D. Y. W. Yu, W. Zhang and C.-S. Lee, *Nano Energy*, 2016, **22**, 27–37.
- 12 Y. Wang, L. Yu and X. W. D. Lou, *Angew. Chem., Int. Ed.*, 2016, **55**, 7423–7426.
- 13 F. Xiong, Z. Cai, L. Qu, P. Zhang, Z. Yuan, O. K. Asare, W. Xu, C. Lin and L. Mai, *ACS Appl. Mater. Interfaces*, 2015, **7**, 12625–12630.
- 14 C.-L. Zhang, Z.-H. Jiang, B.-R. Lu, J.-T. Liu, F.-H. Cao, H. Li, Z.-L. Yu and S.-H. Yu, *Nano Energy*, 2019, **61**, 104–110.
- 15 X. Xia, D. Chao, Z. Fan, C. Guan, X. Cao, H. Zhang and H. J. Fan, *Nano Lett.*, 2014, **14**, 1651–1658.
- 16 X. Zheng, Y. Zheng, H. Zhang, Q. Yang and C. Xiong, *Chem. Eng. J.*, 2019, **370**, 547–555.
- 17 G. Wang, X. Bi, H. Yue, R. Jin, Q. Wang, S. Gao and J. Lu, *Nano Energy*, 2019, **60**, 362–370.
- 18 C. Zhao, C. Yu, M. Zhang, Q. Sun, S. Lia, M. N. Banish, X. Han, Q. Dong, J. Yang, G. Wang, X. Sun and J. Qiu, *Nano Energy*, 2017, **41**, 66–74.
- 19 X. Y. Yu, H. Hu, Y. Wang, H. Chen and X. W. Lou, *Angew. Chem., Int. Ed.*, 2015, **54**, 1–5.



- 20 X. Zhou, L. J. Wan and Y. G. Guo, *Nanoscale*, 2012, **4**, 5868–5871.
- 21 M.-S. Balogun, H. Yang, Y. Luo, W. Qiu, Y. Huang, Z.-Q. Liu and Y. Tong, *Energy Environ. Sci.*, 2018, **11**, 1859–1869.
- 22 H. Zhang, G. Qin, Y. Lin, D. Zhang, H. Liao, Z. Li, J. Tian and Q. Wu, *Electrochim. Acta*, 2018, **264**, 91–100.
- 23 W. Ren, H. Zhang, C. Guan and C. Cheng, *Adv. Funct. Mater.*, 2017, **27**, 1702116.
- 24 T. Wang, C. Sun, M. Yang, G. Zhao, S. Wang, F. Ma, L. Zhang, Y. Shao, Y. Wu, B. Huang and X. Hao, *J. Alloys Compd.*, 2017, **716**, 112–118.
- 25 S. Deng, C. Ai, M. Luo, B. Liu, Y. Zhang, Y. Li, S. Lin, G. Pan, Q. Xiong, Q. Liu, X. Wang, X. Xia and J. Tu, *Small*, 2019, **15**, 1901796.
- 26 S. Deng, M. Luo, C. Ai, Y. Zhang, B. Liu, L. Huang, Z. Jiang, Q. Zhang, L. Gu, S. Lin, X. Wang, L. Yu, J. Wen, J. Wang, G. Pan, X. Xia and J. Tu, *Angew. Chem., Int. Ed.*, 2019, **58**, 16289–16296.
- 27 S. Deng, F. Yang, Q. Zhang, Y. Zhong, Y. Zeng, S. Lin, X. Wang, X. Lu, C. Z. Wang, L. Gu, X. Xia and J. Tu, *Adv. Mater.*, 2018, **30**, e1802223.
- 28 S. Deng, Y. Zhong, Y. Zeng, Y. Wang, X. Wang, X. Lu, X. Xia and J. Tu, *Adv. Sci.*, 2018, **5**, 1700772.
- 29 H. Yu, C. Zhu, K. Zhang, Y. Chen, C. Li, P. Gao, P. Yang and Q. Ouyang, *J. Mater. Chem. A*, 2014, **2**, 4551–4557.
- 30 L. Zeng, S. Chen, J. van der Zalm, X. Li and A. Chen, *Chem. Commun.*, 2019, **55**, 7386–7389.
- 31 L. Zhang, H. B. Wu, Y. Yan, X. Wang and X. W. Lou, *Energy Environ. Sci.*, 2014, **7**, 3302–3306.
- 32 S. Deng, Y. Zhong, Y. Zeng, Y. Wang, Z. Yao, F. Yang, S. Lin, X. Wang, X. Lu, X. Xia and J. Tu, *Adv. Mater.*, 2017, **29**, 1700748.
- 33 H. Liu, X. Chen, L. Deng, X. Su, K. Guo and Z. Zhu, *Electrochim. Acta*, 2016, **206**, 184–191.

